Revisiting the Discrepancy Between Experimental and Theoretical Predictions of the Adiabaticity of $Ti^+ + CH_3OH$

Jennifer R. DeRosa,[*,†,‡] Joseph E. Subotnik,[‡,†] Zheng Pei,[¶] Yihan Shao,[¶] Nicholas S. Shuman,[§] Shaun G. Ard,[§] Albert A. Viggiano,[§] and D. Vale Cofer-Shabica[*,‡]

†*Department of Chemistry, University of Pennsylvania, Philadelphia, Pennsylvania 19104, United States*

‡*Department of Chemistry, Princeton University, Princeton, New Jersey 08544, United States*

¶*Department of Chemistry and Biochemistry, The University of Oklahoma, Norman, Oklahoma 73019, United States*

§*Air Force Research Laboratory, Space Vehicles Directorate, Kirtland Air Force Base, New Mexico 87117, United States*

E-mail: jderosa@sas.upenn.edu; vale@princeton.edu

Abstract

We revisit the naked transition metal cation (Ti^+) and methanol reaction and go beyond the standard Landau-Zener (LZ) picture when modeling the intersystem crossing (ISC) rate between the lowest doublet and quartet states. We use both (i) unconstrained Born–Oppenheimer molecular dynamics (BOMD) calculations with an approximate two-state method to estimate population transfer between spin diabats and

(ii) constrained dynamics to explore energetically accessible portions of the $N_{DOF} - 1$ crossing seam, where N_{DOF} is the total number of internal degrees of freedom. Whereas previous LZ calculations (that necessarily relied on the Condon approximation to be valid) fell short and predicted much slower crossing probabilities than shown in experiment, we show that ISC can occur rapidly because the spin-orbit coupling (SOC) between the doublet and quartet surfaces can vary by two orders of magnitude (depending on where in the seam the crossing occurs during dynamics) and the crossing region is revisited multiple times during a dynamics run of a few hundred femtoseconds. We further isolate the two important nuclear coordinates that tune the SOC and modulate the transition, highlighting exactly how and why organometallic ISC can occur rapidly for small systems with floppy internal nuclear vibrational modes.

Introduction

For transition metals with incompletely filled valence shells, electronic states of varying total electron spin often lie close in energy. Subtle changes in the atom's immediate environment, e.g. a change in coordination or in the nature of a ligand, can cause a reordering of those electronic states. Adiabatic pathways in transition-metal containing reactions are commonly not spin-conserved, and facile ISC between states of differing multiplicity is critical to many transition metal-mediated catalytic processes. Predictive understanding of such catalytic processes is of obvious significance but far from currently achievable with most materials of interest today. In fact, even for small transition metal-containing systems, representative of isolated active sites, predictive understanding of the spin dynamics is usually not achievable today, though such problems do represent a more practical goal than larger complexes with multiple active sites. Significant experimental investigation into these phenomena in ion-molecule reactions extends back to the 1980's. Armentrout and co-workers conducted a series of elegant experiments showing different reactivities of ground and excited spin states of transition metal cations when accounting for differences in total energy and differentiated

systems proceeding on a single spin surface or with crossing between spin surfaces.[1–13] Weisshaar and co-workers attributed reactivity in suprathermal V^+ + alkane reactions to ISC.[14] Schwarz, Shaik, and co-workers subsequently popularized these concepts under the moniker "two-state reactivity" or "multi-state reactivity," detailing numerous instances of the gas-phase phenomena and linking them to solution-phase mechanisms such as for enzymatic oxidations by the P-450 cytochrome.[15–24] While experimental investigation can determine likely mechanistic aspects for a model system, general conclusions are difficult to reach. Ideally, to start making progress, small systems should be studied using reliable quantum chemical methods.

Unfortunately, theoretical efforts on transition-metal bimolecular reactions have lagged. As early as 1988, calculations by Carter and Goddard implicitly recognized that transition metal reactions may be enabled by accessing lower energy transition states on potential surfaces of differing multiplicity.[25] With modern methods, a description of small systems including many electronic states along a single reaction coordinate is readily achievable but probing reactive dynamics (either direct dynamics or trajectory calculations) remain difficult: one requires (i) an accurate description of all relevant portions of the potential energy surface and (ii) an accurate treatment of ISCs. Both of these requirements have proven challenging.

An ideal comparison to experimentally-determined kinetics (e.g. reaction rate coefficients and product branching fractions) requires chemical accuracy (i.e. errors in the calculated energies of less than 1 kcal mol^{-1}, 0.05 eV) in the rate-determining portions of the potential surface. Errors of just 0.1 eV in a rate-limiting transition state energy can cause order-of-magnitude error in the resulting rate coefficient. Thus, such an ideal comparison is infeasible. After all, by necessity, the only affordable electronic structure approach is usually density functional theory (DFT)—for which bond dissociation energies of diatomic molecules with 1st row transition metal atoms calculated using common functionals with a triple-zeta basis set have 2σ uncertainties of greater than 1 eV.[26–28] Coupled cluster calculations like CCSD(T) can reduce the uncertainty of single-reference methods, but this method is not currently

tractable for very large molecules–and in any event, ground-state spin crossovers are difficult to treat with coupled cluster methods.[29–32] In principle, we would like to explore potential energy surfaces with robust multi-reference methods, but this is an exceptionally expensive task for even very small systems.

Moreover, even with an accurate surface, running nonadiabatic dynamics pose a further challenge. Both LZ surface hopping algorithms and Tully's fewest-switches hopping algorithm have seen use in recent years, with the latter having a firmer theoretical foundation.[33] In either case, transition probabilities rely on nonadiabatic coupling elements, which rely on the accuracy and completeness of the surface (in addition, for some multi-reference approaches, nonadiabatic couplings remain very difficult to compute.[34]) At the end of the day—given the realistic constraints on the possible level of electronic structure—in order to model spin-crossovers (even for small metallic systems), it is still unclear what level of approximation is sufficient and then again most efficient.

Despite these grounds for strong concern, there have been some successes. For the $FeO^+ + H_2 \rightarrow Fe^+ + H_2O$ system, Harvey and co-workers calculated a full potential energy surface using DFT along with empirical corrections to force the potential to more closely match established values where known.[35,36] Trajectories were propagated using the fewest-switches surface hopping method, and transition probabilities dictated by SOCs calculated at stationary points and interpolated along the reaction coordinate. The trajectory results align reasonably well with the experimental and statistical modeling results:[37,38] concluding that the entrance well crossing is efficient, that the reaction is instead transition state limited on the quartet surface, and that the exit well crossing is inefficient with 85% of trajectories producing the $^4Fe^+$ product at low energies. Such agreement between the trajectory calculations and the statistical modeling is satisfying; indeed, the "big-picture" statistical modeling results validate the microscopic trajectory results, which can provide detailed dynamical and mechanistic information. Notably, even for this relatively simple transition metal reaction, a large amount of effort and intuition was required to generate a surface that

could reproduce experimental results—but is was fortuitous that a functional was available that well-reproduced the rate-limiting transition state energy. More recently, Guo and co-workers calculated a global potential energy surface for the lowest energy singlet, triplet, and quintet states of the $Ta^+ + CO_2$ and $Nb^+ + CO_2$ reactions.[39–42] Their surfaces were fit to points calculated using a DFT method (selected based on good agreement with CCSD(T) and multi-reference configuration interaction (MRCI) calculations at a limited number of stationary points) along with adjustments for long-range interactions based on simple electrostatic potentials. SOCs were calculated using MRCI at selected points and generalized (assumed to be constant) throughout the surface. The resulting trajectory calculations effectively replicates both kinetic and dynamic experimental results and shows reasonable agreement with statistical modeling.[43] Both of the efforts (i.e. of Harvey and co-workers and Guo and co-workers) are successes, but the significant amount of chemical intuition required to produce the surfaces along with the necessary computational approximations remind us that experimental confirmation is needed for most theoretical predictions.

The study of the activation of methanol by a titanium cation, $Ti^+ + CH_3OH$, is a cautionary tale.[44] Calculation of the complicated reaction coordinate identified a critical barrierless post-rate determining transition state ISC point where the ground state quartet state crosses with an excited state doublet along the major reaction pathway (C−O activation).[45] A small SOC constant was calculated at this point, and therefore, the crossing was deemed inefficient. An inaccessible crossing implied one of two things–either (i) there would be minimal formation of the $TiO^+ + CH_4$ product on the ground state doublet surface ($\approx 1\%$) as compared to the $TiOH^+ + CH_3$ product on an excited quartet surface along the C−O activation pathway ($\approx 99\%$) or that (ii) the $TiO^+ + CH_4$ products would form via an endothermic pathway on an excited quartet surface. Experimental results were at odds with both (i) and (ii), showing a facile ISC and formation of ground state TiO^+ ($\approx 16\%$ compared to $TiOH^+$ formation at 600K) via the exothermic pathway because there was only a weak negative temperature dependence. The calculation methods employed were crude compared to the

approaches described above, but for what reason did they fail? Would calculation of a global PES, similar to the effort of Guo and co-workers, but reliance on coupling constants calculated at selected points have been more successful? More generally, given computational costs, there is always a conundrum about whether to sample more points on inexpensive surfaces or to sample fewer points on more expensive surfaces, and both approaches clearly have merit. In this paper, we will take the former approach, and revisit the $Ti^+ + CH_3OH$ system with trajectory calculations that can more thoroughly explore the potential surface. We employ a novel electronic SHAKE (E-SHAKE) algorithm that can statistically sample the crossing seam and evaluate the propensity for a spin-crossover over a range of energetically accessible geometries. We also run trajectory calculations starting at the transition state and are biased toward products and obtain a rough estimate of the total rate of spin transition. Overall, our results demonstrate that, by way of two concurrent calculations for the different spin-states and for properly sampled dynamics, theory is roughly able to match the corresponding dynamics of this small transition metal-containing complex. Overall, the take-home points of this study are (i) that the magnitude of the SOC can and usually does vary dramatically with geometry for small metallic clusters[46] and (ii) spin crossovers can therefore be much faster than one often anticipates, especially because multiple crossings will frequently occur in small systems without a bath – where decoherence will inevitably be slower.[47,48]

Methods

Computing SOC Between Two Ground State Solutions

At each geometry, we calculated two distinct sets of molecular orbitals corresponding to (i) the quartet and (ii) the doublet spin-restricted DFT solutions. Using such different references inevitably complicates the evaluation of SOC matrix elements because the orbitals do not necessarily have an orthogonality condition. Nevertheless, this obstacle can be overcome by

utilizing a singular value decomposition (SVD) to form two bi-orthogonal MO basis sets.[49] See the appendix for more detail.

Now, for a pair of electron systems with spin quantum numbers S and S' (and $2S+1$ and $2S'+1$ degenerate states characterized by different m_s values in the range of $[-S, S]$ and $[-S', S']$), one often seeks as an averaged SOC between two states, with the most obvious approach being the root mean square:

$$V_{\mathrm{SOC}} = \sqrt{\frac{1}{SS'} \sum_{m_s} \sum_{m'_s} \left| \left\langle \Psi_{S,m_s} \middle| \hat{H}_{\mathrm{SO}} \middle| \Psi'_{S',m'_s} \right\rangle \right|^2} \tag{1}$$

This averaged quantity ignores the phases of the SOC matrix element, but should give a reliable magnitude. For a one-electron operator, a non-vanishing coupling requires that $|S - S'|$ equal 1 or 0, and similarly that $|m_s - m'_s|$ equal 1 or 0. For the problem at hand in this paper, our focus is on ISC where $|S - S'| = 1$, so let us now assume $S' = S + 1$ without loss of generality, and let us further define n_α and n_β as the numbers of α and β electrons in the high spin configuration (so that $m_s \equiv \frac{1}{2}(n_\alpha - n_\beta) = s$). In terms of doublet ($S = 1/2, 2S+1 = 2$) and quartet ($S' = 3/2, 2S'+1 = 4$) couplings, there are three independent (complex) numbers among six terms in total, as shown in Fig. 1(a). For all details regarding how these states are constructed and the matrix elements evaluated, see the appendix.

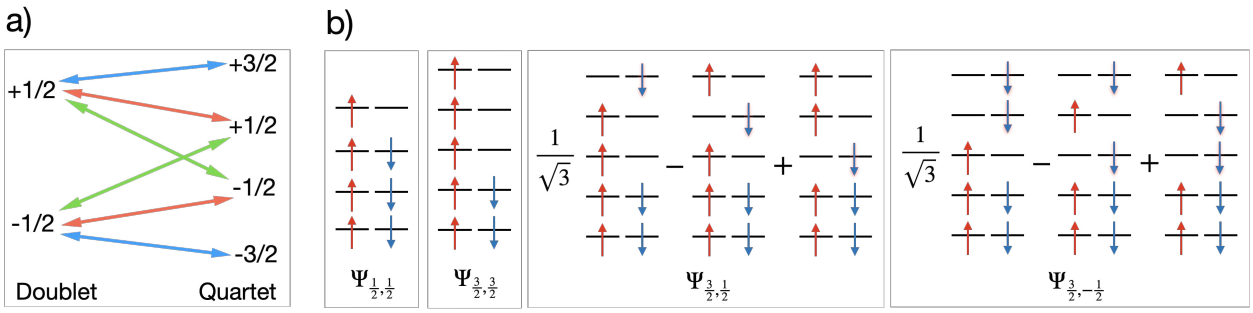

Figure 1: (a) The six SOCs between the two doublet and four quartet states; (b) The determinants diagrams by molecular orbital representations of the $\Psi_{\frac{1}{2},\frac{1}{2}}$ doublet and $\Psi_{\frac{3}{2},\frac{3}{2}}$, $\Psi_{\frac{3}{2},\frac{1}{2}}$, and $\Psi_{\frac{3}{2},-\frac{1}{2}}$ quartets.

For our choice of spin-orbit (SO) operator, we use the one-electron Breit-Pauli (BP) Hamiltonian[50]

$$\hat{H}_{\mathrm{SO}} = -\frac{\alpha_0^2}{2} \sum_i^n \left(\sum_A^N \frac{Z_A}{\left| \vec{r}_i - \vec{R}_A \right|^3} \left(\vec{r}_i - \vec{R}_A \right) \times \vec{p}_i \right) \cdot \vec{s}_i = \sum_i^n \vec{L}_i \cdot \vec{s}_i, \tag{2}$$

where α_0 is the fine structure constant; $\vec{R}_A$ and Z_A are the Cartesian coordinates and nuclear charge of A-th nucleus; $\vec{r}_i$, $\vec{p}_i$, and $\vec{s}_i$ are the coordinates, momentum, and spin of the i-th electron, respectively; and n (N) labels the total number of electrons (nuclei).

Geometry Optimizations, Transition States, and the Reaction Path

All calculations were carried out with a (spin-pure) restricted DFT ansatz using the hybrid functional B3LYP and the def2-TZVP basis set. To begin our analysis, we replicated previous calculations[45] that isolated the transition state and stationary points along the major reaction pathway of Ti^+ and methanol; see Fig. 2. Of particular interest is the portion of the reaction pathway between the transition state on the quartet surface (J) and the stationary point that lies directly to the right hand side of the transition state, leading towards product formation (K). To find this portion of the reaction pathway, we focused on the quartet transition state (J) shown in Fig. 3. From this geometry, we found the nearest minima by perturbing the nuclear geometry along the normal mode corresponding to the imaginary frequency (see Fig. 3), followed by a standard geometry optimization to converge to the local minimum (K) on the quartet surface. Thereafter, we computed the minimum energy path between the two geometries via the freezing string method.[51,52] The region between the transition state (J) and the next minimum (K) is where the ground state quartet surface crosses with the ground state doublet surface.

Sampling the Seam

Whereas previous studies of the $Ti^+ + CH_3OH$ system evaluated only a single SOC at a given geometry, we sought to explore if and how the SOC changed with geometry over the $N_{\mathrm{DOF}} - 1$ dimensional crossing seam between the doublet and quartet surfaces, N_{DOF} being the total number of internal degrees of freedom. For the 7-atom system under consideration (and removing net translation and rotation) the crossing seam is a 14-dimensional manifold. To sample such a seam, we employ a variation on the SHAKE algorithm,[53,54] the standard algorithm which is typically used to constrain molecular geometries (bond lengths and angles) during dynamics. For our purposes, however, we impose a fixed gap (of zero) between the electronic surfaces—this represents an *electronic* constraint and so we will label this an electronic-SHAKE or E-SHAKE approach. We also employ the RATTLE extension to SHAKE,[55] which enhances SHAKE's stability properties and enables us to use a thermostat to sample the seam more efficiently. E-SHAKE has been implemented in INAQS,[56] an open-source software package for nonadiabatic QM/MM simulations that bridges the open-source molecular dynamics package GROMACS[57–59] and the electronic structure package Q-Chem.[60] The INAQS repository contains a modified GROMACS in order to run the E-SHAKE dynamics. The essence of the algorithm is described below, but interested readers should refer to ref. 61 for more details.

The main idea of E-SHAKE is to propagate molecular dynamics:

$$\ddot{\vec{R}} = -\mathbf{M}^{-1} \cdot \vec{\nabla} V \Big|_{\vec{R}} \tag{3}$$

where $(\mathbf{M})_{\mu i,\nu j} = \delta_{ij} m_i$ is the diagonal matrix of masses of each of the N atoms ($i, j \in 1 \ldots N \quad \mu, \nu \in \{x, y, z\}$) and $V(\vec{R})$ is the a potential energy surface, while respecting con-

straints of the form

$$0 = \sigma(t) = \sigma(\vec{R}(t)) \tag{4}$$

$$0 = \dot{\sigma}(t) = \dot{\vec{R}}(t) \cdot \vec{\nabla}\sigma\Big|_{\vec{R}(t)}. \tag{5}$$

Here, the constraint

$$\sigma(\vec{R}) = E_{\mathrm{D}}(\vec{R}) - E_{\mathrm{Q}}(\vec{R}), \tag{6}$$

encodes the difference between the energy of the doublet, E_{D}, and the quartet, E_{Q} at the geometry $\vec{R}$. Eq. 4 ensures that the system remains in the seam of intersection between the doublet and quartet surfaces while Eq. 5 ensures that the velocity at each step is also directed within the seam; for arbitrary σ, Eqs. 4 and 5 are generalizations of the SHAKE and RATTLE conditions respectively.

Under the above constraints, the differential equation for our dynamics, Eq. 3, is modified to include forces of constraint that depend on the Lagrange multipliers introduced to satisfy Eqs. 4 and 5:

$$\ddot{\vec{R}} = -\mathbf{M}^{-1} \cdot \vec{\nabla} V\Big|_{\vec{R}} + \mathbf{M}^{-1} f(\vec{R}; g, k) \tag{7}$$

where g and k are Lagrange multipliers.

We have implemented an algorithm to solve for the Lagrange multipliers so as to propagate 7 while satisfying the constraint (Eq. 6) to arbitrary accuracy. For the purposes of this investigation, we enforce a tolerance of $\left|\sigma(\vec{R})\right| < 4 \times 10^{-5}\,\mathrm{a.u.} \approx 1\,\mathrm{meV}$. Using the above algorithm and the crossing point geometry shown in Fig. 3 as a starting point, we sampled initial velocities according to a Maxwell-Boltzmann distribution at 600K and thermostatted using velocity rescaling with a stochastic term.[62] The dynamics were run for 300 fs with a time step of 0.2 fs. Of course, one should be cautious when interpreting the time reported in Fig. 5 and 6 because such a time scale does not reflect any physically meaningful (observable) dynamics, but rather reflect a statement about how rigorously we have explored and

sampled the seam provided the relevant thermal energy.

Molecular Dynamics and Two-State Approximate Population Transfer

The ultimate means to model barrierless spin-crossover is to run brute-force, *ab initio* dynamical trajectories which automatically explore the relevant parts of the potential energy surface landscape. To that end, it is most natural to start at the transition state when the crossing occurs in the exit channel of the reaction.[63] As such, we initialized a swarm of 38 trajectories beginning at the transition state on the quartet surface (J in Fig. 2) and generated random velocities according to a Maxwell-Boltzmann distribution equivalent to an instantaneous temperature of 600 Kelvin. Additionally, we insured the initial velocities were directed towards products by projecting the velocity vector onto the normal mode corresponding to the imaginary frequency shown in 4 and rejecting any initial condition that gave a negative dot product. During *ab initio* molecular dynamics we used geometric direct minimization (GDM) for robust convergence to the SCF solution. However, since the solution found using GDM can be sensitive to the initial guess,[64] we used the previous step's solution as the initial guess for the current step.

Following dynamics along the quartet surface, we computed the energy of the doublet and the SOCs between the two states at each geometry. Energies and couplings in hand, we built the following reduced two-state electronic Hamiltonian dependent on time via the change in nuclear coordinate.

$$H_{\text{elec}}(\vec{R}) = \begin{bmatrix} E_{\text{D}}(\vec{R}) & \tilde{V}_{\text{SOC}}(\vec{R}) \\ \tilde{V}_{\text{SOC}}(\vec{R}) & E_{\text{Q}}(\vec{R}) \end{bmatrix} \tag{8}$$

Given our interest in exploring ISCs from a quartet and ending on doublet, in Figs. 6, 7, 8, and 11 below, we will include the density of states of the doublet (i.e. two) and report

$\tilde{V}_{\mathrm{SOC}} = \sqrt{2}\, V_{\mathrm{SOC}}$ from Eq. 1.

In order to estimate the spin-branching, we propagated the time-dependent Schrodinger equation (TDSE) using the Hamiltonian above (Eq. 8). For these simulations we initialized the corresponding two-state wavefunction at time zero to be

$$\psi = \begin{bmatrix} C_{\mathrm{D}} \\ C_{\mathrm{Q}} \end{bmatrix} = \begin{bmatrix} 0 \\ 1 \end{bmatrix}, \tag{9}$$

where the complex coefficient of the doublet state (C_{D}) is zero and the quartet state (C_{Q}) is unity.

Results

Transition State and Reaction Path Near Crossing Along Dominant Reaction Pathway

The potential energy surface for the two dominant pathways is shown in Fig. 2. The reactants (H), entrance well (I), and transition state (J) of the quartet surface are lower in energy than the corresponding geometries for the doublet (A, B and C). Fig. 4 shows the normal mode of the imaginary frequency at the transition state on the quartet surface (J). The nuclear displacement of this normal mode shows a change in the distance between the carbon and the oxygen. After the transition state (J), there is a crossing point (CP) between the two spin states and thereafter the doublet has a lower energy. We have characterized the potential energy surface in this region (between J and K in Fig. 3) using the freezing string method. As suggested by Zhang *et. al.*,[45] in order for the adiabatic product (G) to be formed, the system must readily undergo ISC in this region. A SOC calculation at the point where the two surfaces cross (as dictated by the freezing string calculation) reveals a significant spin orbit coupling magnitude (89.8 cm^{-1}). Note that, previous calculations by

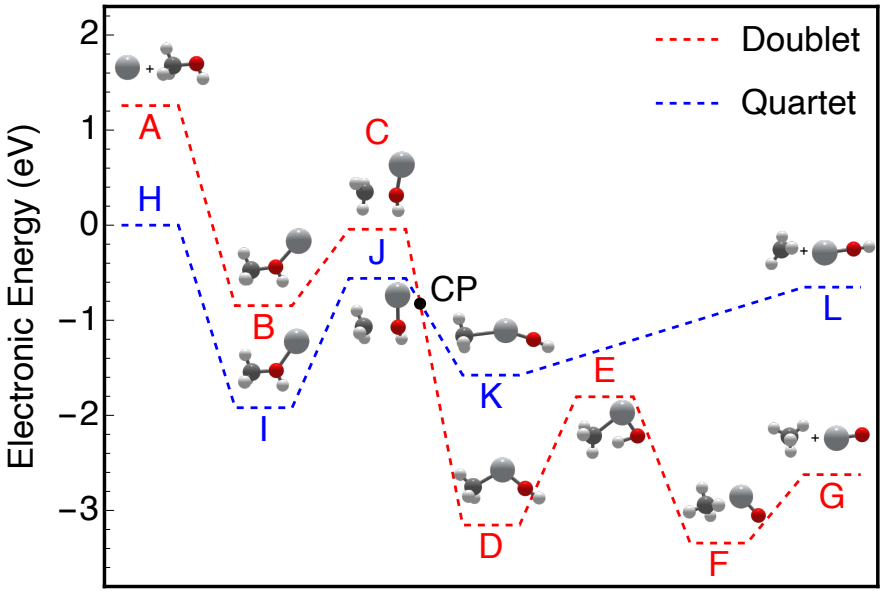

Figure 2: The C-O activation reaction pathway with relevant transition states and intermediates for the doublet and quartet surfaces. Note that, between transition states J on the quartet and intermediate D on the doublet, there is a crossing point (CP) where there is a change in the spin of the ground state.

Zhang *et. al.* found the SOC at the crossing point along the intrinsic reaction coordinate to be small (9.2 cm^{-1}) (with a CASSCF ansatz) which corresponds to only a 1% crossing probability.[45]

Inevitably, one must question: why have we found such a different magnitude of SOC? One might conjecture that this results from a difference in electronic structure approach – which is certainly possible. For example, in our own experience with this problem, the SOC between states can depend very strongly on the choice of active space. That being said, it is also important to emphasize that ref. 45 evaluated the SOC at the (hopefully unique) minimum energy crossing point, whereas we have evaluated the coupling at the crossing point that is conjectured by the freezing string method (with 20 nodes) which might be more physically meaningful dynamically. Most importantly, it is crucial to emphasize that (i) the seam is 14-dimensional and therefore the dynamical implications of a curve-crossing can only be assessed by sampling the relevant space; we will follow this approach in the

next section. Beyond seam sampling, (ii) the most rigorous approach for understanding barrierless ISC (that can explore significantly more of the potential energy surface) is to run *ab initio* dynamics starting from the correct initial coordinates or to evaluate equilibrium reaction rates by starting dynamics from the transition state and following each trajectory; these nonadiabatic dynamics are difficult but progress in this vein will be reported in the dynamics section below.

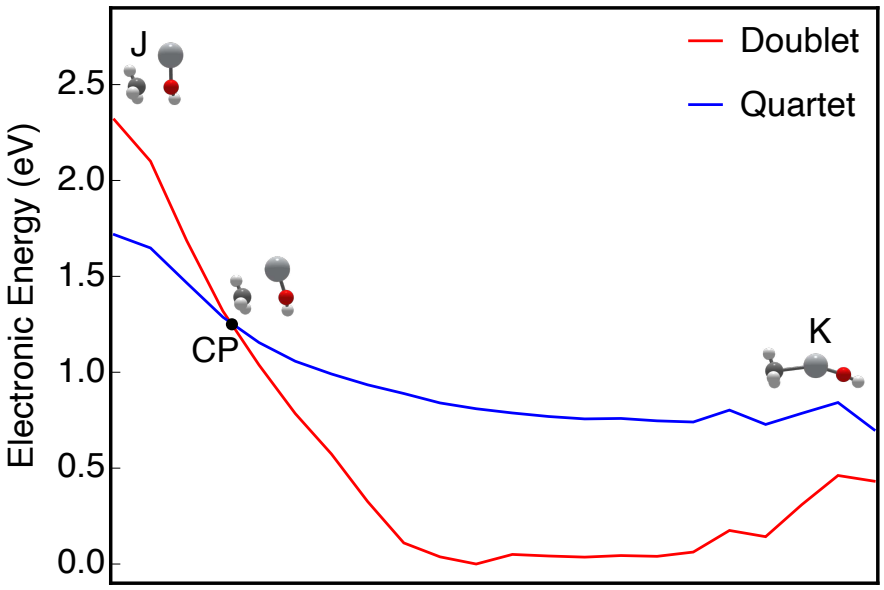

Figure 3: The relative potential energy surfaces of the quartet (blue) and the doublet (red) along the minimum energy pathway from the quartet transition state (J) and the quartet intermediate (K) corresponding to the labels in Fig. 2. The nuclear configuration at the crossing point (CP) is shown.

Seam Sampling: SOC Inside the Seam

In Fig. 5, we plot the magnitude of the SOC between the spin diabats (quartet and doublet) as a function of the fictitious seam-sampling time described above. The electronic energy of the doublet and quartet state (they are necessarily degenerate in the seam) are shown in Fig. 6. Over the course of 300 fs, one observes that the SOC varies by two orders of magnitude, descending as low as 1.7 cm^{-1} and reaching as high as 94.8 cm^{-1} over the course

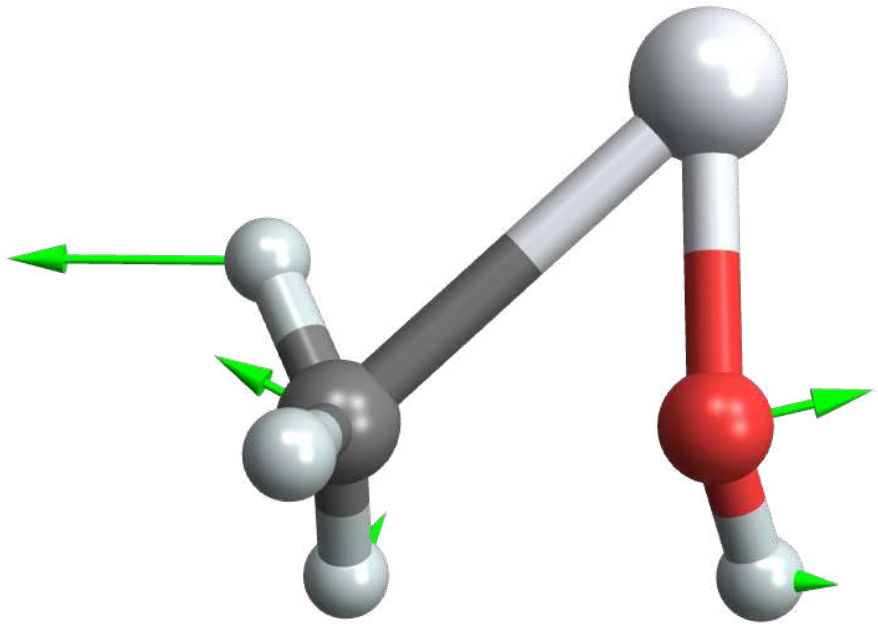

Figure 4: The transition state geometry (J) with the normal mode displacement vector corresponding to the imaginary frequency is plotted in green. Nuclear displacement in this direction pushes the reaction toward intermediate (K).

of the trajectory. Fig. 5 also shows clear oscillations of the SOC magnitude that has a period of approximately 45 fs. Such an oscillatory SOC calls into question the validity of the Condon approximation (which assumes constant SOC). If the Condon approximation is insufficient, then to better understand the resulting ISC, we need to gain intuition regarding the underlying reason for such fluctuations in the coupling. We address the impact of accounting for or excluding such a nuclear dependence in the next section when directly running dynamics.

To that end, the first item of interest is to note that the magnitude of the SOC is reasonably correlated with the relative potential energy of the electronic states. To demonstrate such a correlation, in Fig. 7, we provide a scatter plot of the magnitude of the SOC versus the relative potential energy. For these simulations, our initial point (as chosen by the freezing string method) was quite high in energy (approx. 0.48 eV above the minimum crossing point), and the relative energy decreased rapidly during seam sampling. (For these simulations, the zero of electronic energy is taken as the minimum energy sampled.) From

the data in Fig. 7, we find that there are two distinct regions of configuration space with effectively different couplings; those regions are highlighted by R1 (low-energy region) and R2 (high-energy region). Clearly, one would like to understand why these two regions give such different SOC values. Ultimately, SOC is a matter of conservation of angular momentum. Put simply, if the spin of an electron is to flip during ISC, then the Hamiltonian (which now includes the SO operator Eq. 2) must conserve angular momentum by changing the electronic orbital. That being said, in this work we assess what nuclear coordinates modulate the coupling magnitude in these two regimes with the understanding that these coordinates control the electronic orbitals and their capacity to undergo ISC and conserve angular momentum in line with El-Sayed's rule.[65]

To that end, we have plotted (unshown) the dependence of the SOC on many different possible reaction coordinates. After a great deal of analysis, our assessment is that the main determinants of the SOC are two nuclear coordinates: (i) the the distance from the oxygen's H atom to the C−Ti−O plane and (ii) the C−Ti−O angle (respectively, ζ and θ in Fig. 8(a)). Fig. 8(b) shows the magnitude of the SOC versus the ζ coordinate. Clearly, the value of this nuclear coordinate is correlated and partly determinative of the values of the SOC, especially in the R1 region. Note that the oscillations in the coupling seen in the time-series data (Fig. 5) loosely correlates with the ζ parameter shown in R1.

Next, we turn to the C−Ti−O angle, θ, which is plotted by the color of the point in Fig. 8(b). Clearly, the value of θ dictates a clear difference between the R1 and R2 regions. R1 corresponds to low-energy, large C−Ti−O angles where the molecule is more planar. Meanwhile, R2 includes high-energy and small C−Ti−O angle configurations. At large enough C−Ti−O angles (greater than 160 degrees) this correlation breaks down, and V_{SOC} clearly depends weakly on some other nuclear coordinates, but nevertheless, the dependence of V_{SOC} on ζ and θ is clear from Fig. 8(b).

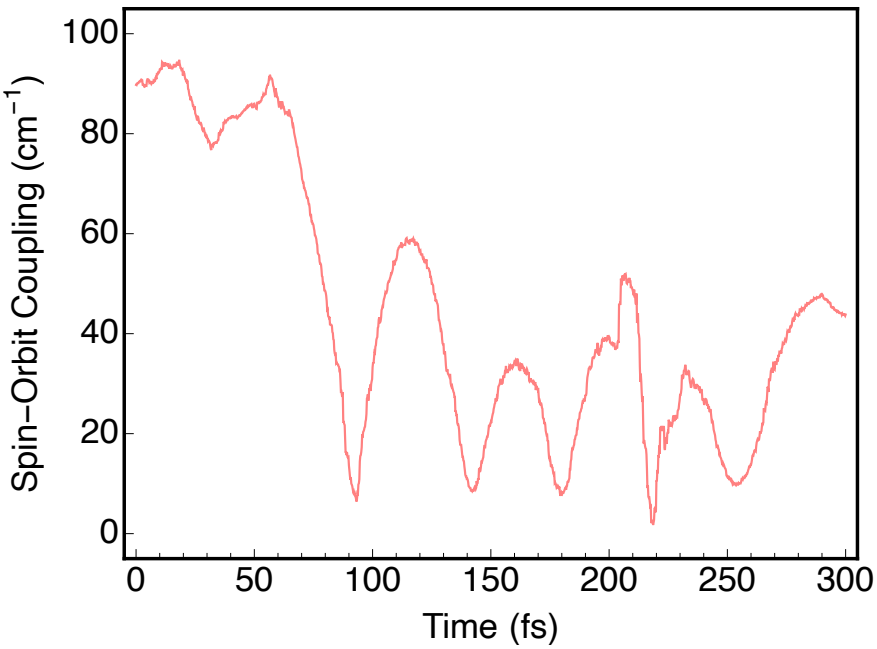

Figure 5: The magnitude of the SOC between the quartet and doublet state during seam sampling at 600K. Note that the magnitude is highly oscillatory and spans between 1.7 cm^{-1} and 94.8 cm^{-1} during the 300 fs.

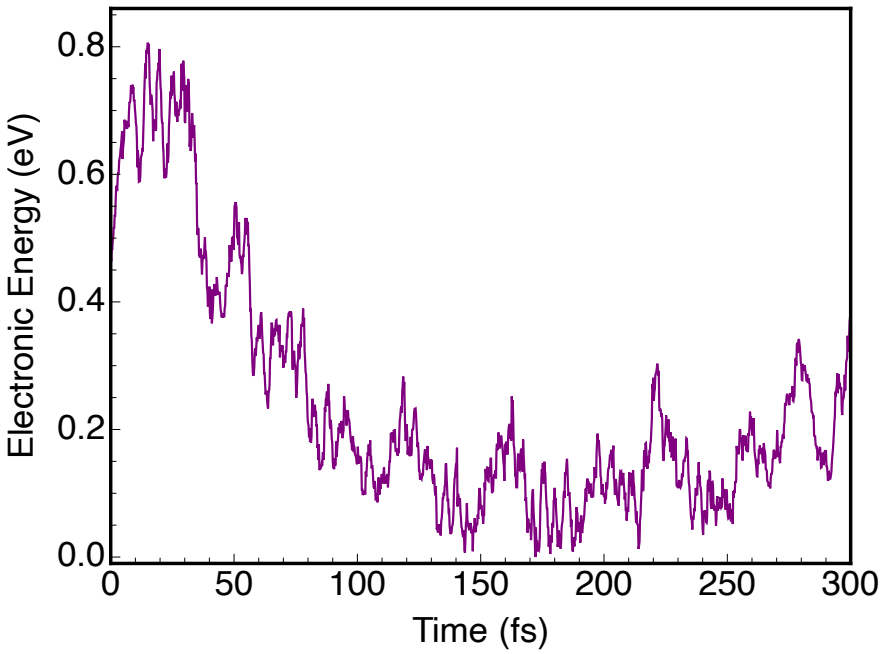

Figure 6: The relative electronic energy of the degenerate doublet and quartet during seam sampling at 600K. The initial configuration has higher energy (0.48 eV) relative to the lowest energy configuration sampled later in the dynamics.

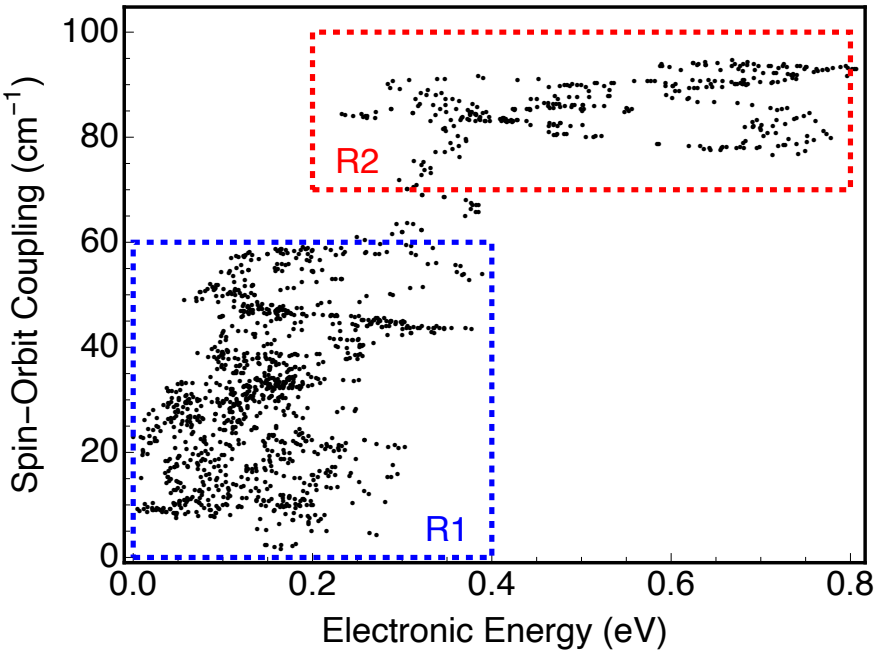

Figure 7: The SOC versus the electronic energy of the degenerate doublet and quartet states during seam sampling at 600K. Notice that the sampling data is separated by two regions: a region where the SOC is smaller with lower energy (R1) and a region where the SOC is larger with higher energy (R2).

Dynamics: Population Transfer Along BOMD Trajectory

Finally, we turn to physically meaningful dynamics. In Fig. 9(a), we report the electronic energy for the doublet and quartet along a sample trajectory run over a total of 300 fs starting at the quartet transition state (and with momentum toward products). In Fig. 9(b) and 9(c), we report the corresponding population of the doublet and the SOC between states, respectively. All crossing points are indicated by a large yellow dot. Interestingly, we find that these resulting dynamics pass through the crossing region multiple times over the span of the short trajectory (seven times in 300 fs in Fig. 9). Each crossing point in Fig. 9(a) has a sufficient SOC to cause a change in the doublet amplitude, but it is also true that using constant coupling (as determined by an average of all reactive trajectories) shows a similar transfer to the doublet state in Fig. 9(b). Clearly, the effect of such coherent dynamics cannot represented by a simple LZ curve crossing problem; with multiple crossings, the change in populations can become quite large and require explicit dynamics to solve.

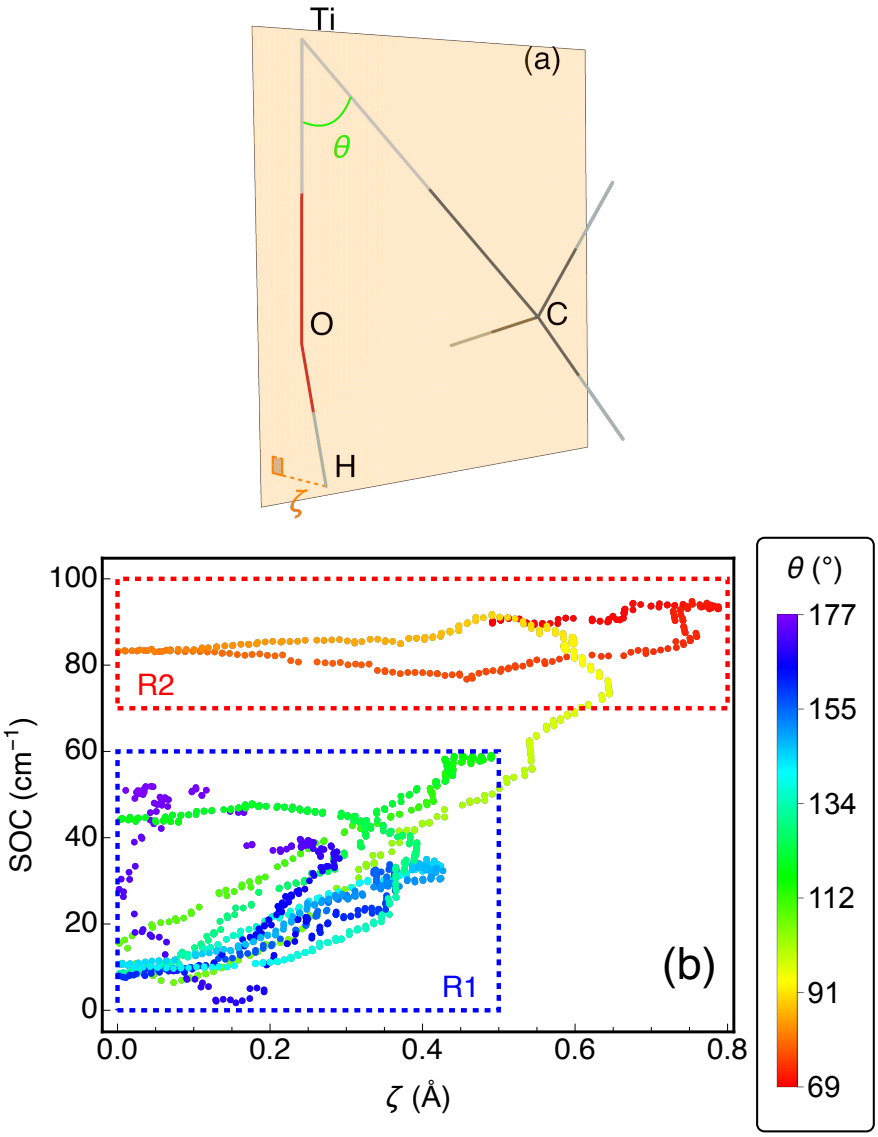

Figure 8: (a) The two key nuclear coordinates that tune the SOC; ζ: the distance of the oxygen's hydrogen from the C-Ti-O plane; θ: C-Ti-O angle; (b) The magnitude of the SOC between the doublet and the quartet states as a function of ζ. The color bar indicates the value of θ at each geometry. Region R1 and R2 from Fig. 7 have large θ and small θ, respectively. Geometries in R1 also show a ζ correlation with the SOC.

Now, the results in Fig. 9 reflect only a single trajectory, and in order to gain more confidence, we should really sample a swarm of trajectories. To that end, we have run 38 such *ab initio* trajectories. In Fig. 10, we plot the final population in the doublet state at the end of the 300 fs for each of the 38 BOMD trajectories. While many of the trajectories resulted in significant population transfer to the doublet (revisiting the crossing region many times), some of the trajectories do not have a large doublet population after 300 fs. For some of these trajectories, there is no such population simply because the surfaces do not cross. In fact, of the 38 trajectories we sampled (each with a positive dot product along the imaginary normal mode that heads toward the crossing point), ten (10) trajectories reverted back to the reactant well (I), as shown by the grey data in Fig. 10. Including only reactive trajectories, the average population transfer at 300 fs is 9.0%. Clearly this data again reflects the important notion that potential energy surfaces and transition states are multidimensional and complex, and one-dimensional, LZ inspired theories will have limitations when the crossing region is barrierless and large portions of the potential energy surface in the crossing region are explored.

Finally, let us return to the large fluctuations in SOC as found during seam-sampling dynamics in Fig. 5, which strongly suggested the limitation of a Condon approximation if the coupling is evaluated only at a single geometry. As we noted in the previous section, one must be careful not to confuse constrained seam-sampling dynamics with physical unconstrained dynamics. That being said, to study the utility of seam sampling more generally as far as simulating reactive dynamics, in Fig. 11, we plot a histogram of the SOC for all 38 trajectories when sampling either (i) the entire trajectory (reactive or non-reactive) or (ii) those regions of configuration space where the energy gap is less than 10 meV (which mimics the sampling space). We find that the average SOC where the gap is small (70.4 cm^{-1}) is similar to the SOC averaged in time during reactive trajectories (64.9 cm^{-1}) with the former being more localized (standard deviation 14.2 cm^{-1}) in the seam vs. 22.2 cm^{-1} overall). Interestingly, the average SOC for non-reactive trajectories is even larger (101.4 cm^{-1}) with

a correspondingly large standard deviation of 25.5 cm^{-1}. For comparison, we also plot the distribution of the SOC during the seam sampling shown in Fig. 5, showing the bimodal distribution for regions R1 and R2 from Figs. 7 and 8. Overall, the conclusion from this data is that, for an accurate prediction of ISC dynamics, one should really sample many different nuclear geometries (as the SOC varies strongly).

Discussion, Future Work, and Conclusions

In conclusion, we have used a novel E-SHAKE algorithm to achieve seam sampling for $Ti^+ + CH_3OH$ ISC scattering, and we have found clear evidence that the SOC varies strongly with position, and we have further identified the relative nuclear coordinates that modulate that coupling, namely the C-Ti-O angle and the distance ζ as shown in Fig. 8(a). Furthermore, we have run *ab initio* BOMD simulations that offer insight into the nature of the ISC dynamics, specifically the possibility of revisiting of a crossing region numerous times in a 300 fs dynamics run. Thus, we posit that the $Ti^+ + CH_3OH$ reaction dynamics cannot be easily modeled by a traditional one-dimensional LZ theory. Returning to the basic theme of the introduction, we hypothesize that, there may not be a substitute for brute-force numerical simulations if we seek to understand ISC in small organometallic systems with barrierless ISC events. That being said, given the computational cost of running dynamics and incorporating the nuclear coordinate dependence of SOC for nonadiabatic dynamics, and in light of the success of Guo and coworkers using a generalized SOC (averaged over select points as in the $Ta^+ + CO_2$ reaction) while running dynamics,[39] it is also possible that using an average SOC during dynamics (or potentially within a sophisticated transition state theory) may not lead to substantial discrepancies (which is supported by our findings in Fig. 9(b)). As we highlighted in the introduction, there is always a tension between the desire for more sampling versus more accurate potential energy surfaces, and there is no clear best approach for all cases.

Looking forward, one can certainly improve on the present calculations. For instance, we have employed the hybrid functional B3LYP and the def2-TZVP basis set for the calculations in this work, but the limitations of DFT are well known, and one can always improve results with CASSCF/MRCI. Using a cheaper electronic structure methods in this work afforded us the opportunity to run long-time dynamics, but it may be worth the cost in the future to verify the results. Perhaps more interestingly, we have invoked a two-state treatment of the doublet and quartet states above, but in reality there is a 6 state crossing and the diabatic couplings have signs and phases (that are ignored in Eq. 1). One must wonder whether significant information is lost when treating the crossing only as a two-state one; indeed, given the recent focus on spin dynamics in electron, transfer[66,67] understanding the distribution of m_s values on the outgoing double channels would be of great theoretical (if not practical) interest.

For future progress, however, the most immediate need is to go beyond BOMD. Note that, in this article, we have estimated population transfer to the doublet state in a crude fashion with no feedback to the nuclear dynamics; we always propagate according to the quartet potential energy surface. Looking forward, if we want to go beyond transition state theory[47,68,69] a more reliable and meaningful approach is to match the nuclear forces with the instantaneous electronic state and account for non-BO (nonadiabatic) effects. To that end, one can imagine running Ehrenfest, fewest-switches surface hopping dynamics,[70–72] or *ab initio* multiple spawning.[73–75] Given the small number of exit channels for this reaction, we must still expect that trajectories will revisit a crossing region several times,[76–78] but the details of the ISC event (and the branching ratios) may well be different with more accurate forces. In general, running nonadiabatic trajectories for ISC trajectories can be quite difficult for several reasons; (i) with degenerate spin states, the choice of hopping states is not well-defined for the surface hopping algorithm; (ii) the derivative couplings are complex-valued and therefore momentum hops or spawning momenta[79] are not well-defined either; (iii) the usual BO dynamics do not conserve linear or angular momentum;[80] (iv)

conical intersection seams in molecules with odd numbers of electrons and spin-orbit coupling are high dimensional and difficult to calculate accurately.[81–85] Despite these limitations, developing new techniques for ISC nonadiabatic dynamics, especially so-called phase space surface hopping techniques,[86–88] is an active area of research in our group and we hope to report results in the future.

Despite all of the limitations above, our seam sampling and dynamics results can largely explain the relative branching ratios found for the $Ti^+ + CH_3OH$ reaction between the two major products $TiO^+ + CH_4$ and $TiOH^+ + CH_3$, highlighting the failures of a simple LZ treatment (especially if one invokes the Condon approximation and evaluates the SOC at a single nuclear configuration) and emphasize the need for new, robust nonadiabatic dynamics methodologies. Looking forward, the E-SHAKE methodology here is available in the current INAQS,[56] and in the future, we believe a simple approach of (i) sampling the seam and then (ii) spawning trajectories from the seam (or if relevant from a nearby transition state) should offer a reasonable fast path forward for explaining a slew of organometallic reactions (starting with those mentioned in the introduction).

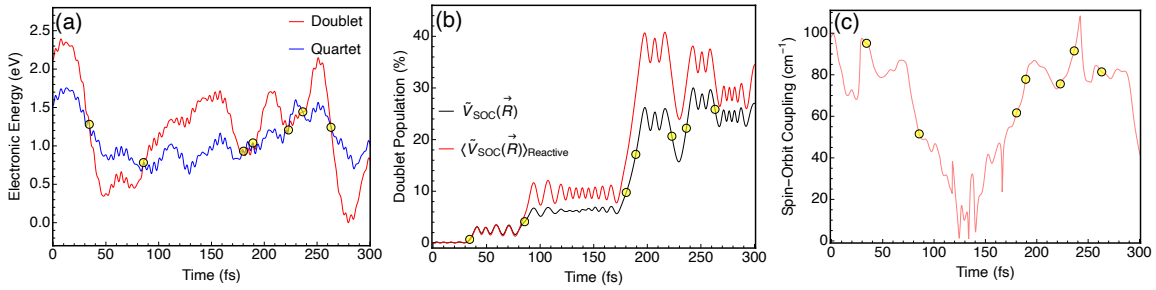

Figure 9: (a) Potential energy surface of the doublet (red) and quartet (blue) along a sample BOMD trajectory confined to the quartet surface. (b) The population transfer to the doublet as dictated by integrating the time-dependent Schrodinger equation using the reduced two-state Hamiltonian in Eq. 8 coupled with the instantaneous SOC (black) or constant SOC as determined by the average SOC of all reactive trajectories (red). (c) The spin-orbit coupling along the trajectory. As expected, large changes in the doublet population occur in regions where the surfaces cross, but perhaps unexpectedly, crossings occur quite often and repeatedly.

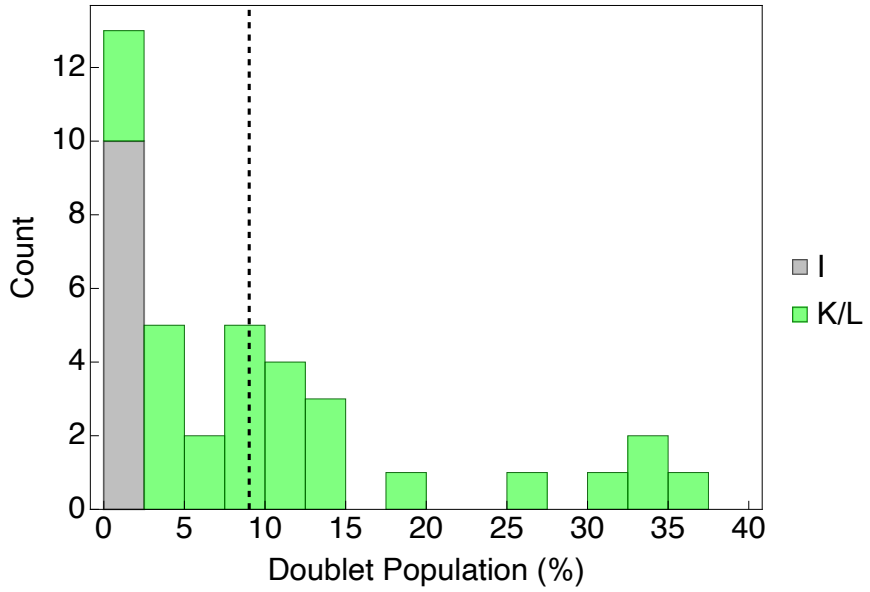

Figure 10: A histogram of the population on the doublet state (according to the wavefunction analysis of ψ in Eq. 9 evolving according to the Hamiltonian in Eq. 8) at the end of the 38 BOMD trajectories. Note that 10 trajectories were nonreactive and returned to the input well, (I). Of the reactive trajectories (in green) that reached points J and K, the average population (dashed black line) being 9.0% at the end of the 300 fs.

Supporting Information

Details on calculating SOC matrix elements between two spin states with different MOs.

Acknowledgements

AFRL authors are supported by the Air Force Office of Scientific Research under AFOSR-22RVCOR009. The views expressed are those of the authors and do not reflect the official guidance or position of the Department of the Air Force, the Department of Defense, or the U.S. government. This material is based upon work supported by the National Science Foundation Graduate Research Fellowship under Grant No. DGE-2236662. The implementation of SOC calculations (Z.P. and Y.S.) was partly supported by the National Science Foundation Grant No. CHE-2102071. Any opinion, findings, and conclusions or recommendations expressed in this material are those of the authors(s) and do not necessarily reflect

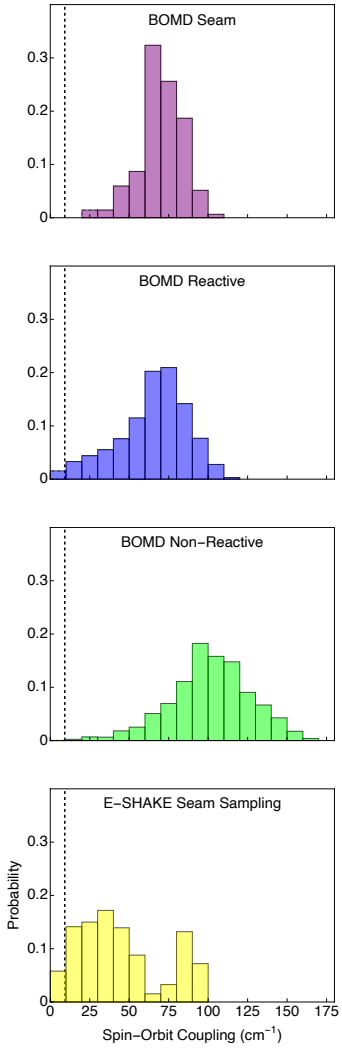

Figure 11: A histogram of the consolidated SOC magnitude during the 38 trajectories for the following: (purple) anytime during the dynamics where the doublet/quartet energy gap was below 10 meV, (blue) all dynamics that were reactive (reached points J and K from Fig. 2), (green) all dynamics that were nonreactive and reverted back to product (I from Fig. 2), and (yellow) during the E-SHAKE seam-sampling dynamics. There is a vertical dashed line at 9.2 cm^{-1}, the previously reported coupling at the minimum energy crossing point by Zhang *et. al.* with CASSCF.[45] Notice that the reactive BOMD and the BOMD in the seam have similar SOC distribution.

the views of the National Science Foundation. This work was supported by the U.S. Air Force Office of Scientific Research (USAFOSR) under Grant Nos. FA9550-23-1-0368 and FA9550-18-1-420. We acknowledge the DoD High Performance Computing Modernization Program for computer time. We thank Yanze Wu for running the CASSCF calculations in Molpro.

References

(1) Kickel, B. L.; Armentrout, P. B. Guided Ion Beam Studies of the Reactions of Ti^+, V^+, and Cr^+ with Silane. Electronic State Effects, Comparison to Reactions with Methane, and M^+–SiHx (x= 0-3) Bond Energies. *Journal of the American Chemical Society* **1994**, *116*, 10742–10750.

(2) van Koppen, P. A.; Bowers, M. T.; Fisher, E. R.; Armentrout, P. Relative energetics of CH and CC Bond activation of alkanes: reactions of Ni^+ and Fe^+ with propane on the lowest energy (adiabatic) potential energy surfaces. *Journal of the American Chemical Society* **1994**, *116*, 3780–3791.

(3) Schröder, D.; Schwarz, H.; Clemmer, D. E.; Chen, Y.; Armentrout, P.; Baranov, V. I.; Böhme, D. K. Activation of hydrogen and methane by thermalized FeO^+ in the gas phase as studied by multiple mass spectrometric techniques. *International journal of mass spectrometry and ion processes* **1997**, *161*, 175–191.

(4) Armentrout, P. B.; Haynes, C. L.; Tjelta, B. L.; Chen, Y. State-specific chemistry of atomic and ligated transition metal ions. Laser Techniques for State-Selected and State-to-State Chemistry III. 1995; pp 258–266.

(5) Chen, Y.; Clemmer, D.; Armentrout, P. Conversion of CH_4 to CH_3OH: Reactions of CoO^+ with CH_4 and D_2, Co^+ with CH_3OD and D_2O, and $Co^+(CH_3OD)$ with Xe. *Journal of the American Chemical Society* **1994**, *116*, 7815–7826.

(6) Aristov, N.; Armentrout, P. Methane activation by V^+: electronic and translational energy dependence. *Journal of Physical Chemistry* **1987**, *91*, 6178–6188.

(7) Schultz, R. H.; Armentrout, P. Nonadiabatic behavior of a transition metal system: exothermic reactions of $Fe^+(^6D, ^4F)$ and propane. *Journal of Physical Chemistry* **1987**, *91*, 4433–4435.

(8) Elkind, J.; Armentrout, P. State-specific reactions of atomic transition-metal ions with H_2, HD, and D_2: effects of d orbitals on chemistry. *Journal of Physical Chemistry* **1987**, *91*, 2037–2045.

(9) Elkind, J.; Armentrout, P. Effect of kinetic and electronic energy on the reactions of Co^+, Ni^+, and Cu^+ with H_2, HD, and D_2. *Journal of Physical Chemistry* **1986**, *90*, 6576–6586.

(10) Georgiadis, R.; Armentrout, P. Translational and electronic energy dependence of the reaction of Mn^+ with ethane. *International journal of mass spectrometry and ion processes* **1989**, *91*, 123–133.

(11) Loh, S.; Fisher, E. R.; Lian, L.; Schultz, R. H.; Armentrout, P. State-specific reactions of $Fe^+(^6D, ^4F)$ with O_2 and c-C_2H_4O. *The Journal of Physical Chemistry* **1989**, *93*, 3159–3167.

(12) Sunderlin, L.; Armentrout, P. Methane activation by Ti^+: electronic and translational energy dependence. *The Journal of Physical Chemistry* **1988**, *92*, 1209–1219.

(13) Schultz, R. H.; Elkind, J.; Armentrout, P. Electronic effects in CH and CC bond activation. State-specific reactions of Fe^+ (^6D, ^4F) with methane, ethane, and propane. *Journal of the American Chemical Society* **1988**, *110*, 411–423.

(14) Sanders, L.; Hanton, S. D.; Weisshaar, J. C. Total reaction cross sections of electronic

state-specified transition metal cations: V^{++} C_2H_6, C_3H_8, and C_2H_4 at 0.2 eV. *The Journal of chemical physics* **1990**, *92*, 3498–3518.

(15) Schröder, D.; Shaik, S.; Schwarz, H. Two-state reactivity as a new concept in organometallic chemistry. *Accounts of Chemical Research* **2000**, *33*, 139–145.

(16) Shaik, S.; Danovich, D.; Fiedler, A.; Schröder, D.; Schwarz, H. Two-state reactivity in organometallic gas-phase ion chemistry. *Helvetica chimica acta* **1995**, *78*, 1393–1407.

(17) Schwarz, H.; Shaik, S.; Li, J. Electronic effects on room-temperature, gas-phase CH Bond activations by cluster oxides and metal carbides: The methane challenge. *Journal of the American Chemical Society* **2017**, *139*, 17201–17212.

(18) Shaik, S.; De Visser, S. P.; Ogliaro, F.; Schwarz, H.; Schröder, D. Two-state reactivity mechanisms of hydroxylation and epoxidation by cytochrome P-450 revealed by theory. *Current opinion in chemical biology* **2002**, *6*, 556–567.

(19) Danovich, D.; Shaik, S. Spin-orbit coupling in the oxidative activation of H−H by FeO^+. Selection rules and reactivity effects. *Journal of the American Chemical Society* **1997**, *119*, 1773–1786.

(20) Bärsch, S.; Schröder, D.; Schwarz, H.; Armentrout, P. Methane to methanethiol conversion by FeS^+. A combined experimental and theoretical study. *The Journal of Physical Chemistry A* **2001**, *105*, 2005–2014.

(21) Rue, C.; Armentrout, P.; Kretzschmar, I.; Schröder, D.; Harvey, J. N.; Schwarz, H. Kinetic-energy dependence of competitive spin-allowed and spin-forbidden reactions: V^{++} CS_2. *The Journal of chemical physics* **1999**, *110*, 7858–7870.

(22) Kretzschmar, I.; Schröder, D.; Schwarz, H.; Rue, C.; Armentrout, P. Experimental and theoretical studies of vanadium sulfide cation. *The Journal of Physical Chemistry A* **1998**, *102*, 10060–10073.

(23) Schröder, D.; Schwarz, H. C-H and C-C Bond Activation by Bare Transition-Metal Oxide Cations in the Gas Phase. *Angewandte Chemie International Edition in English* **1995**, *34*, 1973–1995.

(24) Fiedler, A.; Schroeder, D.; Shaik, S.; Schwarz, H. Electronic structures and gas-phase reactivities of cationic late-transition-metal oxides. *Journal of the American Chemical Society* **1994**, *116*, 10734–10741.

(25) Carter, E. A.; Goddard III, W. A. Modeling Fischer-Tropsch chemistry. The thermochemistry and insertion kinetics of $ClRuH(CH_2)$. *Organometallics* **1988**, *7*, 675–686.

(26) Johnson, E. R.; Becke, A. D. Communication: DFT treatment of strong correlation in 3d transition-metal diatomics. *The Journal of Chemical Physics* **2017**, *146*, 211105.

(27) Chan, B.; Gill, P. M.; Kimura, M. Assessment of DFT methods for transition metals with the TMC151 compilation of data sets and comparison with accuracies for main-group chemistry. *Journal of chemical theory and computation* **2019**, *15*, 3610–3622.

(28) Ruscic, B. Uncertainty quantification in thermochemistry, benchmarking electronic structure computations, and Active Thermochemical Tables. *International Journal of Quantum Chemistry* **2014**, *114*, 1097–1101.

(29) Aoto, Y. A.; de Lima Batista, A. P.; Kohn, A.; de Oliveira-Filho, A. G. How to arrive at accurate benchmark values for transition metal compounds: Computation or experiment? *Journal of chemical theory and computation* **2017**, *13*, 5291–5316.

(30) Shee, J.; Rudshteyn, B.; Arthur, E. J.; Zhang, S.; Reichman, D. R.; Friesner, R. A. On achieving high accuracy in quantum chemical calculations of 3d transition metal-containing systems: a comparison of auxiliary-field quantum monte carlo with coupled cluster, density functional theory, and experiment for diatomic molecules. *Journal of chemical theory and computation* **2019**, *15*, 2346–2358.

(31) Fang, Z.; Vasiliu, M.; Peterson, K. A.; Dixon, D. A. Prediction of bond dissociation energies/heats of formation for diatomic transition metal compounds: CCSD (T) works. *Journal of chemical theory and computation* **2017**, *13*, 1057–1066.

(32) Cheng, L.; Gauss, J.; Ruscic, B.; Armentrout, P. B.; Stanton, J. F. Bond dissociation energies for diatomic molecules containing 3d transition metals: benchmark scalar-relativistic coupled-cluster calculations for 20 molecules. *Journal of chemical theory and computation* **2017**, *13*, 1044–1056.

(33) Subotnik, J. E.; Ouyang, W.; Landry, B. R. Can we derive Tully's surface-hopping algorithm from the semiclassical quantum Liouville equation? Almost, but only with decoherence. *The Journal of Chemical Physics* **2013**, *139*, 214107.

(34) Park, J. W.; Shiozaki, T. Analytical derivative coupling for multistate CASPT2 theory. *Journal of chemical theory and computation* **2017**, *13*, 2561–2570.

(35) Harvey, J. N.; Tew, D. P. Understanding the reactivity bottleneck in the spin-forbidden reaction $FeO^+ + H_2 \rightarrow Fe^+ + H_2O$. *International Journal of Mass Spectrometry* **2013**, *354*, 263–270.

(36) Essafi, S.; Tew, D. P.; Harvey, J. N. The Dynamics of the Reaction of FeO^+ and H_2: A Model for Inorganic Oxidation. *Angewandte Chemie International Edition* **2017**, *56*, 5790–5794.

(37) Ard, S. G.; Melko, J. J.; Martinez Jr, O.; Ushakov, V. G.; Li, A.; Johnson, R. S.; Shuman, N. S.; Guo, H.; Troe, J.; Viggiano, A. A. Further insight into the reaction FeO++ H2→ Fe++ H2O: Temperature dependent kinetics, isotope effects, and statistical modeling. *The Journal of Physical Chemistry A* **2014**, *118*, 6789–6797.

(38) Ard, S. G.; Johnson, R. S.; Melko, J. J.; Martinez, O.; Shuman, N. S.; Ushakov, V. G.; Guo, H.; Troe, J.; Viggiano, A. A. Spin-inversion and spin-selection in the reactions

$FeO^+ + H_2$ and $Fe^+ + N_2O$. *Physical Chemistry Chemical Physics* **2015**, *17*, 19709–19717.

(39) Liu, Y.; Ončák, M.; Meyer, J.; Ard, S. G.; Shuman, N. S.; Viggiano, A. A.; Guo, H. Multistate Dynamics and Kinetics of CO_2 Activation by Ta^+ in the Gas Phase: Insights into Single-Atom Catalysis. *Journal of the American Chemical Society* **2024**, *146*, 14182–14193.

(40) Liu, Y.; Oncák, M.; Meyer, J.; Ard, S. G.; Shuman, N. S.; Viggiano, A. A.; Guo, H. Intersystem Crossing Control of the Nb++ CO2→ NbO++ CO Reaction. *The Journal of Physical Chemistry A* **2024**, *128*, 6943–6953.

(41) Jiang, B.; Guo, H. Permutation invariant polynomial neural network approach to fitting potential energy surfaces. *The Journal of chemical physics* **2013**, *139*, 054112.

(42) Li, J.; Jiang, B.; Guo, H. Permutation invariant polynomial neural network approach to fitting potential energy surfaces. II. Four-atom systems. *The Journal of chemical physics* **2013**, *139*, 204103.

(43) Huber, M. E.; Lewis, T. W.; Meta, M.; Ard, S. G.; Liu, Y.; Sweeny, B. C.; Guo, H.; Ončák, M.; Shuman, N. S.; Meyer, J. Ta+ and Nb++ CO 2: intersystem crossing in ion–molecule reactions. *Physical Chemistry Chemical Physics* **2024**, *26*, 8670–8680.

(44) Sweeny, B. C.; Ard, S. G.; McDonald, D. C.; Martinez Jr, O.; Viggiano, A. A.; Shuman, N. S. Discrepancy between Experimental and Theoretical Predictions of the Adiabaticity of $Ti^+ + CH_3OH$. *Chemistry–A European Journal* **2017**, *23*, 11780–11783.

(45) Zhang, F.; Guo, W.; Zhao, L.; Lin, X.; Zhang, L.; Zhu, H.; Shan, H. Theoretical survey of the potential energy surface of Ti^+ + methanol reaction. *The Journal of Physical Chemistry A* **2009**, *113*, 7103–7111.

(46) Penfold, T. J.; Gindensperger, E.; Daniel, C.; Marian, C. M. Spin-Vibronic Mechanism for Intersystem Crossing. *Chemical Reviews* **2018**, *118*, 6975–7025, PMID: 29558159.

(47) Jasper, A. W. Multidimensional Effects in Nonadiabatic Statistical Theories of Spin-Forbidden Kinetics: A Case Study of 3O + CO → CO2. *Journal of Physical Chemistry A* **2015**, *119*, 7339–7351, PMID: 25871914.

(48) Jasper, A. W.; Nangia, S.; Zhu, C.; Truhlar, D. G. Non-Born-Oppenheimer Molecular Dynamics. *Accounts of Chemical Research* **2006**, *39*, 101–108, PMID: 16489729.

(49) Chiodo, S. G.; Leopoldini, M. MolSOC: A spin–orbit coupling code. *Computer Physics Communications* **2014**, *185*, 676–683.

(50) Tao, Y.; Pei, Z.; Bellonzi, N.; Mao, Y.; Zou, Z.; Liang, W.; Yang, Z.; Shao, Y. Constructing spin-adiabatic states for the modeling of spin-crossing reactions. I. A shared-orbital implementation. *International Journal of Quantum Chemistry* **2019**, *120*, e26123.

(51) Behn, A.; Zimmerman, P. M.; Bell, A. T.; Head-Gordon, M. Efficient exploration of reaction paths via a freezing string method. *The Journal of chemical physics* **2011**, *135*, 224108.

(52) Mallikarjun Sharada, S.; Zimmerman, P. M.; Bell, A. T.; Head-Gordon, M. Automated transition state searches without evaluating the Hessian. *Journal of chemical theory and computation* **2012**, *8*, 5166–5174.

(53) Ryckaert, J.-P.; Ciccotti, G.; Berendsen, H. J. Numerical integration of the cartesian equations of motion of a system with constraints: molecular dynamics of n-alkanes. *Journal of computational physics* **1977**, *23*, 327–341.

(54) Ciccotti, G.; Ryckaert, J.-P. Molecular dynamics simulation of rigid molecules. *Computer Physics Reports* **1986**, *4*, 346–392.

(55) Andersen, H. C. Rattle: A "velocity" version of the shake algorithm for molecular dynamics calculations. *Journal of computational Physics* **1983**, *52*, 24–34.

(56) Cofer-Shabica, D. V.; Menger, M. F.; Ou, Q.; Shao, Y.; Subotnik, J. E.; Faraji, S. INAQS, a generic interface for nonadiabatic QM/MM dynamics: design, implementation, and validation for GROMACS/Q-CHEM simulations. *Journal of Chemical Theory and Computation* **2022**, *18*, 4601–4614.

(57) Berendsen, H. J.; van der Spoel, D.; van Drunen, R. GROMACS: A message-passing parallel molecular dynamics implementation. *Computer physics communications* **1995**, *91*, 43–56.

(58) Hess, B.; Kutzner, C.; Van Der Spoel, D.; Lindahl, E. GROMACS 4: algorithms for highly efficient, load-balanced, and scalable molecular simulation. *Journal of chemical theory and computation* **2008**, *4*, 435–447.

(59) Pronk, S.; Páll, S.; Schulz, R.; Larsson, P.; Bjelkmar, P.; Apostolov, R.; Shirts, M. R.; Smith, J. C.; Kasson, P. M.; Van Der Spoel, D.; others GROMACS 4.5: a high-throughput and highly parallel open source molecular simulation toolkit. *Bioinformatics* **2013**, *29*, 845–854.

(60) Epifanovsky, E.; Gilbert, A. T.; Feng, X.; Lee, J.; Mao, Y.; Mardirossian, N.; Pokhilko, P.; White, A. F.; Coons, M. P.; Dempwolff, A. L.; others Software for the frontiers of quantum chemistry: An overview of developments in the Q-Chem 5 package. *The Journal of chemical physics* **2021**, *155*, 084801.

(61) Cofer-Shabica, D. V.; Subotnik, J. E. Seam sampling reveals coupling between electronic and nuclear coordinates in energy excitation transfer complex. **2024**, in preparation.

(62) Bussi, G.; Donadio, D.; Parrinello, M. Canonical sampling through velocity rescaling. *The Journal of chemical physics* **2007**, *126*, 014101.

(63) Li, H.; Kamasah, A.; Matsika, S.; Suits, A. G. Intersystem crossing in the exit channel. *Nature Chemistry* **2019**, *11*, 123–128.

(64) Van Voorhis, T.; Head-Gordon, M. A geometric approach to direct minimization. *Molecular Physics* **2002**, *100*, 1713–1721.

(65) El-Sayed, M. Spin—orbit coupling and the radiationless processes in nitrogen heterocyclics. *The Journal of Chemical Physics* **1963**, *38*, 2834–2838.

(66) Bian, X.; Wu, Y.; Teh, H.-H.; Zhou, Z.; Chen, H.-T.; Subotnik, J. E. Modeling nonadiabatic dynamics with degenerate electronic states, intersystem crossing, and spin separation: A key goal for chemical physics. *The Journal of Chemical Physics* **2021**, *154*, 110901.

(67) Bian, X.; Wu, Y.; Rawlinson, J.; Littlejohn, R. G.; Subotnik, J. E. Modeling spin-dependent nonadiabatic dynamics with electronic degeneracy: A phase-space surface-hopping method. *The Journal of Physical Chemistry Letters* **2022**, *13*, 7398–7404.

(68) Lykhin, A. O.; Kaliakin, D. S.; dePolo, G. E.; Kuzubov, A. A.; Varganov, S. A. Nonadiabatic transition state theory: Application to intersystem crossings in the active sites of metal-sulfur proteins. *International Journal of Quantum Chemistry* **2016**, *116*, 750–761.

(69) Dergachev, V. D.; Rooein, M.; Dergachev, I. D.; Lykhin, A. O.; Mauban, R. C.; Varganov, S. A. NAST: Nonadiabatic statistical theory package for predicting kinetics of spin-dependent processes. *New Horizons in Computational Chemistry Software* **2022**, 79–103.

(70) Richter, M.; Marquetand, P.; González-Vázquez, J.; Sola, I.; González, L. SHARC: ab Initio Molecular Dynamics with Surface Hopping in the Adiabatic Representation Including Arbitrary Couplings. *Journal of Chemical Theory and Computation* **2011**, *7*, 1253–1258.

(71) Mai, S.; Marquetand, P.; González, L. Nonadiabatic dynamics: The SHARC approach. *Wiley Interdisciplinary Reviews: Computational Molecular Science* **2018**, *8*, e1370.

(72) Mai, S.; Marquetand, P.; González, L. A general method to describe intersystem crossing dynamics in trajectory surface hopping. *International Journal of Quantum Chemistry* **2015**, *115*, 1215–1231.

(73) Curchod, B. F.; Martínez, T. J. Ab initio nonadiabatic quantum molecular dynamics. *Chemical reviews* **2018**, *118*, 3305–3336.

(74) Fedorov, D. A.; Pruitt, S. R.; Keipert, K.; Gordon, M. S.; Varganov, S. A. Ab Initio Multiple Spawning Method for Intersystem Crossing Dynamics: Spin-Forbidden Transitions between 3B1 and 1A1 States of GeH2. *The Journal of Physical Chemistry A* **2016**, *120*, 2911–2919, PMID: 27064356.

(75) Fedorov, D. A.; Lykhin, A. O.; Varganov, S. A. Predicting Intersystem Crossing Rates with AIMS-DFT Molecular Dynamics. *The Journal of Physical Chemistry A* **2018**, *122*, 3480–3488, PMID: 29533626.

(76) Jasper, A. W.; Hack, M. D.; Truhlar, D. G. The treatment of classically forbidden electronic transitions in semiclassical trajectory surface hopping calculations. *Journal of Chemical Physics* **2001**, *115*, 1804–1816.

(77) Zhu, C.; Jasper, A. W.; Truhlar, D. G. Non-Born-Oppenheimer trajectories with self-consistent decay of mixing. *Journal of Chemical Physics* **2004**, *120*, 5543–5547.

(78) Zhu, C.; Nangia, S.; Jasper, A. W.; Truhlar, D. G. Coherent switching with decay of mixing: An improved treatment of electronic coherence for non-Born-Oppenheimer trajectories. *Journal of Chemical Physics* **2004**, *121*, 7658–7670.

(79) Martinez, T. J.; Levine, R. D. First-principles molecular dynamics on multiple electronic states: A case study of NaI. *Journal of Chemical Physics* **1996**, *105*, 6334–6341.

(80) Bian, X.; Tao, Z.; Wu, Y.; Rawlinson, J.; Littlejohn, R. G.; Subotnik, J. E. Total Angular Momentum Conservation in Ab Initio Born-Oppenheimer Molecular Dynamics. *Physical Review B* **2023**, *108*, L220304.

(81) Mead, C. A. The "noncrossing" rule for electronic potential energy surfaces: The role of time-reversal invariance. *Journal of Chemical Physics* **1979**, *70*, 2276–2283.

(82) Matsika, S.; Yarkony, D. R. On the effects of spin-orbit coupling on conical intersection seams in molecules with an odd number of electrons. I. Locating the seam. *Journal of Chemical Physics* **2001**, *115*, 2038–2050.

(83) Matsika, S.; Yarkony, D. R. On the effects of spin–orbit coupling on conical intersection seams in molecules with an odd number of electrons. II. Characterizing the local topography of the seam. *Journal of Chemical Physics* **2001**, *115*, 5066–5075.

(84) Matsika, S.; Yarkony, D. R. Spin-orbit coupling and conical intersections in molecules with an odd number of electrons. III. A perturbative determination of the electronic energies, derivative couplings and a rigorous diabatic representation near a conical intersection. *Journal of Chemical Physics* **2002**, *116*, 2825–2835.

(85) Matsika, S.; Yarkony, D. R. Spin-Orbit Coupling and Conical Intersections. IV. A Perturbative Determination of the Electronic Energies, Derivative Couplings, and a Rigorous Diabatic Representation near a Conical Intersection. The General Case. *Journal of Physical Chemistry B* **2002**, *106*, 8108–8116.

(86) Shenvi, N. Phase-space surface hopping: Nonadiabatic dynamics in a superadiabatic basis. *Journal of Chemical Physics* **2009**, *130*, 124117.

(87) Wu, Y.; Rawlinson, J.; Littlejohn, R. G.; Subotnik, J. E. Linear and angular momentum conservation in surface hopping methods. *The Journal of Chemical Physics* **2024**, *160*, 024119.

(88) Tao, Z.; Qiu, T.; Bhati, M.; Bian, X.; Duston, T.; Rawlinson, J.; Littlejohn, R. G.; Subotnik, J. E. Practical phase-space electronic Hamiltonians for ab initio dynamics. *The Journal of Chemical Physics* **2024**, *160*, 124101.

TOC Graphic

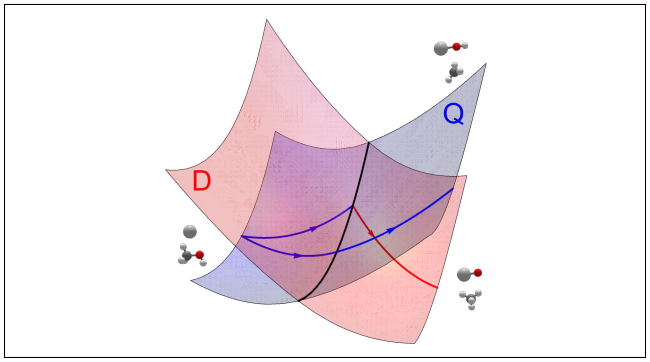

Revisiting the Discrepancy Between Experimental and Theoretical Predictions of the Adiabaticity of $Ti^+ + CH_3OH$

Jennifer R. DeRosa,[*,†,‡] Joseph E. Subotnik,[‡,†] Zheng Pei,[¶] Yihan Shao,[¶] Nicholas S. Shuman,[§] Shaun G. Ard,[§] Albert A. Viggiano,[§] and D. Vale Cofer-Shabica[*,‡]

†*Department of Chemistry, University of Pennsylvania, Philadelphia, Pennsylvania 19104, United States*

‡*Department of Chemistry, Princeton University, Princeton, New Jersey 08544, United States*

¶*Department of Chemistry and Biochemistry, The University of Oklahoma, Norman, Oklahoma 73019, United States*

§*Air Force Research Laboratory, Space Vehicles Directorate, Kirtland Air Force Base, New Mexico 87117, United States*

E-mail: jderosa@sas.upenn.edu; vale@princeton.edu

Calculating SOC Between Two Spin States with Different MOs

Within the representation of canonical molecular orbitals (MOs), ψ, the the BP SO operator (Eq. 2) requires matrix elements of the "scaled" angular momentum integral of the form:

$$\vec{L}_{pq} = i\frac{\alpha_0^2}{2}\left\langle \psi_p \middle| \sum_A^N \frac{Z_A}{\left|\vec{r}-\vec{R}_A\right|^3}\left(\vec{r}-\vec{R}_A\right)\times\boldsymbol{\nabla}\middle|\psi_q\right\rangle. \tag{S1}$$

which is pure imaginary due to the momentum operator, where p and q label occupied orbitals. From these Cartesian components, one can define the corresponding ladder operators $L^{\pm}_{pq}$ and L^0_{pq} as

$$L^{\pm}_{pq} = L^x_{pq} \pm iL^y_{pq}, \qquad L^0_{pq} = L^z_{pq}, \tag{S2}$$

and then Eq. 2 can be reformed into

$$\hat{H}_{\mathrm{SO}} = \frac{1}{2}\sum_{pq}\left(L^+_{pq}\hat{O}^{1,-1}_{pq} - L^-_{pq}\hat{O}^{1,1}_{pq} + L^0_{pq}\hat{O}^{1,0}_{pq}\right), \tag{S3}$$

where the triplet spin-tensor operators are[1]

$$\begin{aligned}
\hat{O}^{1,-1}_{pq} &= a^\dagger_{p\beta}a_{q\alpha},\\
\hat{O}^{1,0}_{pq} &= \frac{1}{\sqrt{2}}\left(a^\dagger_{p\alpha}a_{q\alpha} - a^\dagger_{p\beta}a_{q\beta}\right),\\
\hat{O}^{1,1}_{pq} &= -a^\dagger_{p\alpha}a_{q\beta},
\end{aligned} \tag{S4}$$

in second quantization. $a^\dagger$ and a are the creation and annihilation operators, respectively, and α and β refer to the electron spin (up and down). The calculations in this paper are restricted (α and β orbitals have the same spatial component), but the method described

below is general and can be used in the unrestricted case as well.

When the two electronic states are constructed from the same set of MOs, the summation in Eq. S3 reduces to a sum over singly occupied orbitals because of the orthogonality condition for the MOs; however, if the two states are solved separately through self-consistent procedure, this conclusion does not hold. Nevertheless, a brute sum over orbitals approach can be circumvented by utilizing a singular value decomposition (SVD) to form two bi-orthogonal MO basis sets.[2] Namely, we construct the MO overlap matrices

$$\begin{aligned}
\mathbf{C}_{\mathrm{o}}^{\alpha,\dagger}\mathbf{S}\mathbf{C}_{\mathrm{o}}^{\prime\alpha} &= \mathbf{S}_{\mathrm{oo}}^{\alpha} = \mathbf{U}^{\alpha}\mathbf{d}^{\alpha}\mathbf{V}^{\alpha,\dagger}, \\
\mathbf{C}_{\mathrm{o}}^{\beta,\dagger}\mathbf{S}\mathbf{C}_{\mathrm{o}}^{\prime\beta} &= \mathbf{S}_{\mathrm{oo}}^{\beta} = \mathbf{U}^{\beta}\mathbf{d}^{\beta}\mathbf{V}^{\beta,\dagger},
\end{aligned} \tag{S5}$$

for the α and β electrons, respectively. Here $\mathbf{S}$ is the AO overlap matrix, and $\mathbf{C}_{\mathrm{o}}^{\alpha/\beta}$ and $\mathbf{C}_{\mathrm{o}}^{\prime\alpha/\beta}$ are the α/β occupied MO coefficients of the two states, respectively. $\mathbf{S}_{\mathrm{oo}}^{\alpha}$ has dimensionality $n_\alpha \times n'_\alpha$ where n_α and n'_α are the number of α spins for the two states, respectively. The singular values $\mathbf{d}^{\alpha}$ usually includes $n_{\mathrm{core}}^{\alpha} = \min(n_\alpha, n'_\alpha)$ non-zero elements and $n_0 = |n_\alpha - n'_\alpha| = \left|n_\beta - n'_\beta\right|$ zeros. In such a case, $\mathbf{U}^{\alpha}$ and the first $n_{\mathrm{core}}^{\alpha}$ columns of $\mathbf{V}^{\alpha}$ correspond to the non-zero singular values while the last n_0 columns of $\mathbf{V}^{\alpha}$ would yield null space. Similarly, $\mathbf{S}_{\mathrm{oo}}^{\beta}$ has dimension $n_\beta \times n'_\beta$, where $\mathbf{U}^{\beta}$ is divided into two blocks with $n_{\mathrm{core}}^{\beta} = \min(n_\beta, n'_\beta)$ and n_0 columns, respectively, and $\mathbf{V}^{\beta}$ has $n_{\mathrm{core}}^{\beta}$ columns in total. Hence the two bi-orthogonal orbital coefficient matrices can be represented as

$$\begin{aligned}
\tilde{\mathbf{C}}_{\mathrm{o}}^{\alpha} &= \mathbf{C}_{\mathrm{o}}^{\alpha}\mathbf{U}^{\alpha}, \\
\tilde{\mathbf{C}}_{\mathrm{o}}^{\prime\alpha} &= \mathbf{C}_{\mathrm{o}}^{\prime\alpha}\mathbf{V}^{\alpha} = \mathbf{C}_{\mathrm{o}}^{\prime\alpha}(\mathbf{V}_{n_{\mathrm{core}}^{\alpha}}^{\alpha}, \mathbf{V}_{n_0}^{\alpha});
\end{aligned} \tag{S6}$$

$$\begin{aligned}
\tilde{\mathbf{C}}_{\mathrm{o}}^{\beta} &= \mathbf{C}_{\mathrm{o}}^{\beta}\mathbf{U}^{\beta} = \mathbf{C}_{\mathrm{o}}^{\beta}(\mathbf{U}_{n_{\mathrm{core}}^{\beta}}^{\beta}, \mathbf{U}_{n_0}^{\beta}), \\
\tilde{\mathbf{C}}_{\mathrm{o}}^{\prime\beta} &= \mathbf{C}_{\mathrm{o}}^{\prime\beta}\mathbf{V}^{\beta}.
\end{aligned} \tag{S7}$$

SOC matrix element between $\Psi_{S,S}$ and $\Psi_{S+1,S+1}$

In practice, if one seeks a Slater determinant with a given spin multiplicity S, a quantum chemistry software package usually returns a self-consistent optimized state with the largest m_s value; such states are represented by the first two determinants in Fig. 1(b). The SOC between two such electronic states $\Psi_{S,S}$ and $\Psi'_{S+1,S+1}$ is given by

$$V^{\rm soc}_{S,S;S+1,S+1} = v^{\rm soc}_{+}\Lambda\prod \mathbf{d}^{\alpha}_{\rm core}\mathbf{d}^{\beta}_{\rm core}, \qquad\qquad v^{\rm soc}_{+} = \tilde{\mathbf{C}}^{\beta,\dagger}_{n_0}\mathbf{L}^{+}\tilde{\mathbf{C}}'^{\alpha}_{n_0}. \tag{S8}$$

Here, the determinants of the overlap matrices are replaced by the products of non-zero singular values, with the phase $\Lambda = \det(\mathbf{U}^{\alpha})\det(\mathbf{V}^{\alpha})\det\big(\mathbf{U}^{\beta}\big)\det\big(\mathbf{V}^{\beta}\big) = \pm 1$. The one-electron SOC, $v^{\rm soc}_{+}$, is evaluated from the null space orbitals in Eqs. (S6) and (S7) together with the spin-orbit operator in Eq. (S3), where $\mathbf{L}_{+}$ is the angular momentum integrals in atomic orbital (AO) representation defined by Eqs. (S1) and (S2). Note that, of all of the terms in Eq. (S3), only the L^{+} component (which multiplies $\hat{O}^{1,-1}$) survives because the ket state has an extra α electron compared to the bra state; the other two terms in Eq. (S3) vanish. Note also that, for the coupling between $\Psi_{S,-S}$ and $\Psi'_{S+1,-(S+1)}$, the result is also straightforward; one can flip all spins (up to down and down to up) so that the analogue of Eq. (S8) is still valid but with the matrix $\mathbf{L}^{-}$ (instead of $\mathbf{L}^{+}$):

$$V^{\rm soc}_{S,-S;S+1,-(S+1)} = v^{\rm soc}_{-}\Lambda\prod \mathbf{d}^{\alpha}_{\rm core}\mathbf{d}^{\beta}_{\rm core}, \qquad\qquad v^{\rm soc}_{-} = \tilde{\mathbf{C}}^{\beta,\dagger}_{n_0}\mathbf{L}^{-}\tilde{\mathbf{C}}'^{\alpha}_{n_0}. \tag{S9}$$

SOC matrix element between $\Psi_{S,S}$ and $\Psi_{S+1,S}$

Next, let us address the coupling between states $\Psi_{S,S}$ and $\Psi'_{S+1,S}$; this matrix element is more tricky to compute, as the latter is not a Slater determinant. To form the $\Psi'_{S+1,S}$ wavefunction, we consider the $\Psi'_{S+1,S+1}$ Slater determinant, isolate the (2S+2) α orbitals in this determinant with least overlap to the β orbitals in the same determinant, and then finally flip each orbital appropriate (and with the appropriate sign, see Fig. 1(b)) so as

to achieve a wavefunction with m_s number S (i.e. so that $\Psi'_{S,S}$ and $\Psi'_{S+1,S}$ have the same number of both α and β orbitals). Mathematically, in general, the relevant orbitals are found by constructing the α-β overlap matrix between the α and β orbitals for the $\Psi'_{S+1,S+1}$ Slater determinant, $\mathbf{C}_{\mathrm{o}}'^{\alpha}\mathbf{S}\mathbf{C}_{\mathrm{o}}'^{\beta}$, and then taking the SVD of this matrix: $\mathbf{C}_{\mathrm{o}}'^{\alpha}\mathbf{S}\mathbf{C}_{\mathrm{o}}'^{\beta} = \tilde{\mathbf{U}}\tilde{\mathbf{d}}\tilde{\mathbf{V}}$. As a function of the original AO basis, the desired orbitals are then of the form:

$$\begin{aligned}\tilde{\mathbf{C}}_{\mathrm{o}}''^{\alpha} &= \mathbf{C}_{\mathrm{o}}'^{\alpha}\tilde{\mathbf{U}}, \\ \tilde{\mathbf{C}}_{\mathrm{o}}''^{\beta} &= \mathbf{C}_{\mathrm{o}}'^{\beta}\tilde{\mathbf{V}}.\end{aligned} \tag{S10}$$

Note that the $\mathbf{C}_{\mathrm{o}}'^{\alpha}$ matrix has $(n'_{\alpha} - n'_{\beta})$ more columns than the $\mathbf{C}_{\mathrm{o}}'^{\beta}$ matrix. Note also that this SVD is unnecessary for the case of a restricted calculation (as we have done above), in which case $\mathbf{C}_{\mathrm{o}}'^{\alpha}\mathbf{S}\mathbf{C}_{\mathrm{o}}'^{\beta}$ is nearly the identity matrix (with only a few extra columns of zero), and the core α and β orbitals are identical, so that identifying the α orbitals with no β counterpart is trivial.

The process above has identified which orbitals we will flip when building the low-spin state. For instance, in the case of the high-spin quartet, we will construct a linear combination of three Slater determinants by flipping the spins of three different orbitals (one at a time); again, see 1(b). Let us index each orbital to be flipped by the index k, and let us denote $\tilde{\Psi}_{S+1}^{(k)}$ as the Slater determinant with orbital k flipped from up to down (with MO coefficient matrices $\tilde{\mathbf{C}}_{\mathrm{o}}''^{\alpha(k)}$ and $\tilde{\mathbf{C}}_{\mathrm{o}}''^{\beta(k)}$). In order to construct the SOC matrix element between $\Psi_{S,S}$ and $\tilde{\Psi}_{S+1}^{(k)}$, we line up the α orbitals between these two different Slater determinants and then perform another SVD procedure so as to generate the biorthogonal (or corresponding) orbitals:

$$\mathbf{C}_{\mathrm{o}}^{\alpha,\dagger}\mathbf{S}\tilde{\mathbf{C}}_{\mathrm{o}}''^{\alpha(k)} = \mathbf{S}_{\mathrm{oo}}'^{\alpha(k)} = \mathbf{U}'^{\alpha(k)}\mathbf{d}'^{\alpha(k)}\mathbf{V}'^{\alpha(k)\dagger}. \tag{S11}$$

We repeat this procedure for the β orbitals:

$$\mathbf{C}_{\mathrm{o}}^{\beta,\dagger}\mathbf{S}\tilde{\mathbf{C}}_{\mathrm{o}}^{\prime\prime\beta(k)} = \mathbf{S}_{\mathrm{oo}}^{\prime\beta(k)} = \mathbf{U}^{\prime\beta(k)}\mathbf{d}^{\prime\beta(k)}\mathbf{V}^{\prime\beta(k)\dagger}, \tag{S12}$$

Finally, the effective one-electron SOC between $\Psi_{S,S}$ and $\tilde{\Psi}_{S+1}^{(k)}$ reads:

$$v_{z(k)}^{\mathrm{soc}} = \frac{(-1)^k}{2}\Lambda^{\prime(k)}\left(\left(\mathbf{C}_{\mathrm{o}}^{\alpha}\mathbf{U}_{n_0}^{\prime\alpha(k)}\right)^{\dagger}\mathbf{L}^z\left(\tilde{\mathbf{C}}_{\mathrm{o}}^{\prime\prime\alpha}\mathbf{V}_{n_0}^{\prime\alpha(k)}\right)d_{n_0}^{\prime\beta(k)} - \left(\mathbf{C}_{\mathrm{o}}^{\beta}\mathbf{U}_{n_0}^{\prime\beta(k)}\right)^{\dagger}\mathbf{L}^z\left(\tilde{\mathbf{C}}_{\mathrm{o}}^{\prime\prime\beta}\mathbf{V}_{n_0}^{\prime\beta(k)}\right)d_{n_0}^{\prime\alpha(k)}\right), \tag{S13}$$

where $\Lambda^{\prime(k)} = \det\left(\mathbf{U}^{\prime\alpha(k)}\right)\det\left(\mathbf{V}^{\prime\alpha(k)}\right)\det\left(\mathbf{U}^{\prime\beta(k)}\right)\det\left(\mathbf{V}^{\prime\beta(k)}\right)$ gives the phase of the overlap matrices. Note that we require a phase $(-1)^k$ (i.e. a phase depending on identity of the flipped electron) in order to generate the correct overall low-spin many-body state. The final SOC value between$\Psi_{S,S}$ and $\Psi_{S+1,S}$ is then:

$$V_{S,S;S+1,S}^{\mathrm{soc}} = \frac{1}{\sqrt{n_\alpha^\prime - n_\beta^\prime}}\sum_k\left(v_{z(k)}^{\mathrm{soc}}\prod\mathbf{d}_{\mathrm{core}}^{\prime\alpha(k)}\mathbf{d}_{\mathrm{core}}^{\prime\beta(k)}\right), \tag{S14}$$

where the coefficient is from the average of the determinants. Note that, for the corresponding states constructed by flipping every electron spin (i.e. the time reversal states), we find that:

$$V_{S,-S;S+1,-S}^{\mathrm{soc}} = -V_{S,S;S+1,S}^{\mathrm{soc}}. \tag{S15}$$

SOC matrix element between $\Psi_{S,S}$ and $\Psi_{S+1,S-1}$

There is still one piece left for coupling between $\Psi_{S,S}$ and $\Psi_{S+1,S-1}$ states. Here we would flip two electrons from α to β for the latter state, based on the transformed orbitals in Eq. (S10); and then we have the SVD equations

$$\begin{aligned}\mathbf{C}_{\mathrm{o}}^{\alpha,\dagger}\mathbf{S}\tilde{\mathbf{C}}_{\mathrm{o}}^{\prime\prime\alpha(k)} &= \mathbf{S}_{\mathrm{oo}}^{\prime\prime\alpha(k)} = \mathbf{U}^{\prime\prime\alpha(k)}\mathbf{d}^{\prime\prime\alpha(k)}\mathbf{V}^{\prime\prime\alpha(k)\dagger},\\ \mathbf{C}_{\mathrm{o}}^{\beta,\dagger}\mathbf{S}\tilde{\mathbf{C}}_{\mathrm{o}}^{\prime\prime\beta(k)} &= \mathbf{S}_{\mathrm{oo}}^{\prime\prime\beta(k)} = \mathbf{U}^{\prime\prime\beta(k)}\mathbf{d}^{\prime\prime\beta(k)}\mathbf{V}^{\prime\prime\beta(k)\dagger},\end{aligned} \tag{S16}$$

for each s, which labels the left (unflipped) singly occupied α-orbital among the last $(n'_\alpha - n'_\beta)$ columns. It leads to the one-orbital SOCs

$$v''^{\mathrm{soc}}_{\pm(k)} = (-1)^k \Lambda''^{(k)} \left(\mathbf{C}^{\alpha}_{\mathrm{o}} \mathbf{U}''^{\alpha(k)}_{n_0}\right)^{\dagger} \mathbf{L}^{\pm} \left(\tilde{\mathbf{C}}''^{\beta}_{\mathrm{o}} \mathbf{V}''^{\beta(k)}_{n_0}\right), \tag{S17}$$

with phase factor $\Lambda''^{(k)} = \det\left(\mathbf{U}''^{\alpha(k)}\right) \det\left(\mathbf{V}''^{\alpha(k)}\right) \det\left(\mathbf{U}''^{\beta(k)}\right) \det\left(\mathbf{V}''^{\beta(k)}\right)$, and finally the total SOCs

$$\begin{aligned} V^{\mathrm{soc}}_{S,S;S+1,S-1} &= \frac{1}{\sqrt{n'_\alpha - n'_\beta}} \sum_k v''^{\mathrm{soc}}_{-(k)} \prod \mathbf{d}''^{\alpha(k)}_{\mathrm{core}} \mathbf{d}''^{\beta(k)}_{\mathrm{core}}, \\ V^{\mathrm{soc}}_{S,-S;S+1,-S+1} &= \frac{1}{\sqrt{n'_\alpha - n'_\beta}} \sum_k v''^{\mathrm{soc}}_{+(k)} \prod \mathbf{d}''^{\alpha(k)}_{\mathrm{core}} \mathbf{d}''^{\beta(k)}_{\mathrm{core}} \end{aligned} \tag{S18}$$

of $\Psi_{S,S}$ and $\Psi_{S+1,S-1}$ and of its image states $\Psi_{S,-S}$ and $\Psi_{S+1,-S+1}$, respectively.

References

(1) Pokhilko, P.; Epifanovsky, E.; Krylov, A. I. General framework for calculating spin–orbit couplings using spinless one-particle density matrices: Theory and application to the equation-of-motion coupled-cluster wave functions. *The Journal of Chemical Physics* **2019**, *151*.

(2) Chiodo, S. G.; Leopoldini, M. MolSOC: A spin–orbit coupling code. *Computer Physics Communications* **2014**, *185*, 676–683.